OPTICA

Control and scaling of nonlinear emission for super-resolution microscopy

Kevin Murzyn,[1,3] Tanya W. P. van Horen,[1] and Peter M. Kraus[1,2,*]

[1]Advanced Research Center for Nanolithography, Science Park 106, 1098 XG Amsterdam, The Netherlands
[2]LaserLaB, Department of Physics and Astronomy, Vrije Universiteit Amsterdam, De Boelelaan 1105, 1081 HV Amsterdam, The Netherlands
[3]k.murzyn@arcnl.nl
*p.kraus@arcnl.nl

Received 13 August 2025; revised 8 December 2025; accepted 9 December 2025; published 20 January 2026

Super-resolution microscopy—imaging below the Abbe diffraction limit—was a resounding success in the development of optical far-field microscopy and revolutionized bioimaging. Yet most super-resolution techniques are based on fluorescence microscopy. However, fluorescent labels impose restrictions on implementing this technique in some fields of science. Label-free techniques such as third-harmonic generation (THG) microscopy are an alternative, but only provide limited resolution due to their infrared driver. In this work, we show how to optimize the point-spread function (PSF) of THG microscopes, first for a single-color harmonic driving laser, and then in a two-color field. For a single-color driver, a low input intensity leads to the smallest PSF. This occurs because an effective nonlinear order close to the order of the emitted harmonic leads to the maximum possible spot size reduction of the harmonic emission profile with respect to the incident intensity profile of the driver. In the two-color case, we utilize a second light pulse with a donut-shaped fluence profile in focus, which is generated by introducing orbital angular momentum. We show that this second pulse shrinks the PSF below the diffraction limit. Although there is no principal limit to this shrinkage, meaning that there is no principal limit to resolution in our approach, the current implementation is practically limited by sample damage. Currently, this promises a factor of 4 reduction of the PSF and a concomitant improvement of the resolution by a factor of 4 in a coherent harmonic microscopy imaging system. These findings open the pathway to implement super-resolution techniques in a broader scientific and industrial application, i.e., in condensed-matter physics and for semiconductor wafer metrology.

https://doi.org/10.1364/OPTICA.576385

1. INTRODUCTION

Optical super-resolution microscopy has brought a leap forward in discoveries in the field of biology and medicine [1]. However, most of these techniques require fluorescent markers to work [2]. This renders these techniques incompatible with solid-state physics, semiconductor wafer inspection, and operando microscopy (for instance, for heterogeneous catalysis and in general chemistry monitoring). All of these areas would undoubtedly benefit from experiments with a high spatial resolution, and some also from high temporal resolution.

High-harmonic generation (HHG) is an already established technique in the fields of microscopy and solid-state physics in many different forms, thanks to a myriad of benefits. Harmonic microscopy is a frequently employed technique as harmonic generation offers intrinsic contrast for microscopy because it arises solely from a material's nonlinear optical response, independent of external labels. In bioimaging and pathology, second- and third-harmonic signals highlight structural features such as collagen [3], myosin [4], and lipid interfaces [5,6] with sub-micron specificity and minimal photodamage. For 2D materials, harmonic contrast reveals crystal symmetry, grain boundaries, stacking order, and strain fields [7–9] with nanoscale sensitivity. In nonlinear dielectric metasurfaces, harmonic emission directly maps local field enhancement, modal coupling, and symmetry-engineered selection rules, enabling rapid characterization of resonant behavior [10–12]. Together, these modalities deliver chemically specific, label-free, and ultrafast contrast mechanisms. First, in microscopy, HHG is an energetic up-conversion process, leading to a shorter wavelength of the measured light and therefore to a better resolution. Second, although label-free nanoscopy methods exist, they are based either on near-field techniques [13,14] or access to a large-scale facility [15], making HHG microscopy a far-field tabletop alternative. In a recent study, we introduced the concept of harmonic deactivation microscopy (HADES), which addresses the issue of limited resolution in HHG microscopy [16]. By adding a second donut-shaped deactivation beam similar to conventional super-resolution techniques [17,18], we control the electron-hole dephasing times and recombination probabilities, through which we limit the spatial extent of the harmonic emission below the diffraction limit, which we explore further in the present manuscript.

As a spectroscopic tool, HHG is an inherent attosecond process [19,20], allowing us to observe materials at much shorter timescales compared to fluorescence. This opens the potential to have attosecond temporal and nanometer spatial resolution via HADES.

In this work, we show that HADES is capable of breaking the diffraction limit and achieving super-resolution. We explore the theoretical and experimental limitations of the technique and show that there is no fundamental limit to the resolution with HADES. To show this resolution scaling, we systematically investigate the spot size reduction of the point-spread function (PSF) in a third-harmonic generation (THG) microscope via spatial deactivation. Spatial deactivation refers to controlling the emission with a spatially structured control pulse, which we achieve here by an orbital-angular momentum of one carrying pulse, which in focus generates a donut shape and therefore deactivates HHG everywhere except in the center of the control pulse which carries no intensity. This in turn reduces the PSF. The width of the PSF in a microscope is directly linked to the resolution limit in coherent imaging. Although in principle there is no limit to improving this resolution barrier via HADES, in the present study, the PSF in a THG microscope can be reduced to four times below the diffraction limit. This finite reduction is currently limited by sample damage at even higher deactivation fluences. Thus, both mitigation of laser damage and improved HHG deactivation concepts can further enhance resolution improvement.

In the present work, we first introduce and derive the necessary theory for the expected PSF in THG microscopy and HADES in Section 2. Second, we describe the conducted experiments and used materials in Section 3. Lastly, we present the obtained results for the point-spread function in THG microscopy and HADES, i.e., in one- and two-color laser fields, respectively, in Section 4, and compare those with the theoretical prediction.

2. CONCEPTS AND THEORY FOR RESOLUTION IMPROVEMENT IN HADES

A. Deactivation of High-Harmonic Generation in Two-Color Laser Fields

To understand the deactivation of HHG from solids following photoexcitation, defined as the intensity reduction of the emission, we can learn a lot from the gas HHG process in two-color laser fields. The presence of a second color can control the trajectories and recollision of tunneling electrons [19] and thereby influence the divergence and efficiency of the HHG process [21,22]. Further, HHG is highly susceptible to preexcitation. In molecules, exciting even small fractions of electronic coherences can give rise to very large signal modulations [23], and likewise the alignment or orientation of a molecule can have a major impact on the conversion efficiency [24].

The fundamental similarities between HHG in solids and gases [20] suggest the possibility of accurate quantum control of the emission in solids, as was shown in gases. Excitation with a second pulse prior to or during HHG showed near-unity emission control of HHG in a pantheon of different materials [25–32], most often in the form of deactivating the HHG. While many of these experiments were carried out with pulses that can excite carriers by one-photon transitions, deactivation also occurs by pulses with energies below the band gap, either by multi-photon excitation or by optical cross-modulation during pump-probe overlap. We have reviewed and summarized the recent literature on time-resolved high-harmonic generation from solids in our recent perspective article [33] and found that deactivation of HHG is a general phenomenon. The physical mechanism of deactivation of HHG originates mainly from two effects, which we recap here from [33]. First, during pulse overlap, the two overlapping colors create a new waveform. Particularly when composed of incommensurate frequencies, this can cause a suppression of HHG. While a detailed investigation is still pending, deactivation during pulse overlap in a two-color field can be thought to originate from breaking and lowering the periodicity of the generating field which therefore suppresses the generation of particular harmonic frequencies. Second, after pulse overlap, excited electrons cause an increase in scattering, which results in a decrease in the electron-hole coherence dephasing time. Electron-hole coherence is essential to the coherent emission in high-harmonic generation, thus any decrease in dephasing time (or equivalently, any increase in the scattering rate) will lead to a suppression of the amplitude of HHG emission [34]. Therefore, deactivation of HHG is expected to occur in most, and if optimized, practically all materials [33]. In the specific case of NbO_2, the control pulses also trigger an insulator-to-metal phase transition [32]. The two different material phases also have different HHG efficiencies, both due to their different band structures, and due to different scattering rates akin to the mechanism described above. Finally we note that effects like state blocking due to excited electrons may play a role as well; however at the relatively low excitation densities typically encountered in semiconductors and present in the current paper, we do not assign high importance to this effect. The HHG deactivation behavior after pulse-overlap can be seen in the temporal behavior of the THG from NbO_2 in Fig. 1A. Here, a sudden drop in overall intensity is followed by a slow recovery. Further, with higher powers of the second beam, the yield drops lower (Fig. 1B) until it reaches zero. The normalized deactivation δ can be empirically modeled by an exponential saturation model with a harmonic order m dependent saturation fluence $\Phi_{\mathrm{sat},m}$ as

$$\delta(\Phi) = 1 - \exp\left(-\ln(2)\Phi/\Phi_{\mathrm{sat},m}\right), \tag{1}$$

where Φ_{sat} is the deactivation fluence at which the emission is halved. In Fig. 1C, we show that this model fits our experimental data very well. This model is motivated by the exponential decrease of the HHG yield for reduced dephasing times [34,35], and the inherent near-linear decrease of dephasing times arising from excited carrier population [36,37]. The consequence is an exponential decrease of the HHG yield as a function of fluence in the deactivation pulse as derived theoretically in Ref. [34], and experimentally verified in Refs. [26,30]. In previous studies [26,32,34], it was shown both experimentally and theoretically that higher harmonics deactivate at a lower deactivation fluence, or expressed differently, that higher harmonics deactivate more strongly at a given fluence. This can be rationalized within the semiclassical picture where carrier acceleration in the bands underlies HHG. Higher harmonics are typically accelerated for longer. Therefore, they are more strongly suppressed by scattering, which is enhanced by photoexcited carriers in the present study. This means that while the deactivation of HHG due to increased electron-hole decoherence after excitation is generally valid, the exact value of the deactivation fluence is material-dependent. However, as we show later, a phenomenological adherence to the exponential saturation model is enough for an accurate prediction of the resolution.

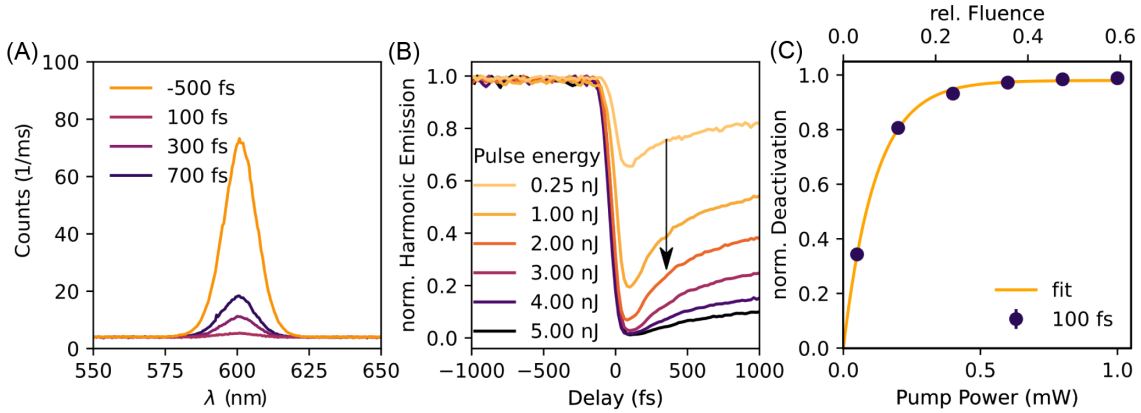

Fig. 1. Deactivation of HHG by prepulses in NbO_2. (A) When a pump pulse arrives simultaneously or before the excitation pulse, high-harmonic generation is suppressed. (B) The minimum harmonic emission in NbO_2 occurs 100 fs after the pump pulse arrives. Here, with increasing pulse energies, the harmonic emission decreases. (C) Plotting the normalized deactivation of THG (1 corresponds to full suppression, i.e., no harmonic emission) as a function of pump power at a time delay of maximum deactivation (100 fs) allows us to fit an exponential saturation model to the power dependence. The top axis of the relative fluence is normalized to the damage threshold fluence of the pump beam under the same focusing conditions.

B. Theoretical Limits of Resolution Improvement by HADES

We now derive how the spatial deactivation of high-harmonic generation in solids is achieved by pre-exciting a sample. To understand the scaling of resolution in HADES, we first need to understand the resolution of an HHG microscope. In HHG microscopy, a near-infrared laser generates harmonics from the sample of interest in focus, where the intensity relation in the perturbative model is described as

$$I_{\mathrm{HG}} \propto I_{\mathrm{NIR}}^{m_{\mathrm{eff}}}, \tag{2}$$

where m_{eff} is the effective nonlinear order, which in the perturbative limit corresponds to the actual order m of the harmonic process. Even for higher, non-perturbatively generated harmonics, a power law relation typically still holds, but saturation occurs at higher intensities and the effective nonlinear order becomes generally lower than the actual harmonic order. Assuming a Gaussian spatial intensity distribution in the NIR focus spot $I_{\mathrm{NIR}}(r) \propto \exp(-4\ln(2) r^2/d_0^2)$, we can describe the HHG intensity profile with (2) as

$$I_{\mathrm{HG}}(r) \propto \exp\left(-4\ln(2)\frac{r^2}{(d_0/\sqrt{m_{\mathrm{eff}}})^2}\right), \tag{3}$$

where $d_0 = \lambda_{\mathrm{ex}}/(2\mathrm{NA})$ is the full width at half-maximum (FWHM) after Abbe's diffraction limit of the original NIR beam at wavelength λ_{ex}, and NA is the numerical aperture of the focusing objective. From the FWHM of Eq. (3), a modified Abbe's diffraction limit for HHG microscopy is given by

$$d_m = \frac{\lambda_{\mathrm{ex}}}{2\mathrm{NA}\sqrt{m_{\mathrm{eff}}}}. \tag{4}$$

This modification is visualized in Fig. 2A. Compared to the fundamental driver, the THG has a smaller PSF.

The deactivating pulse—i.e., the HADES pulse—carries orbital angular momentum (OAM) and thus has a donut shape in focus. We model the electric field as a $\sin^2$ fluence distribution (Fig. 2B) after Refs. [18,38]. Through a first-order Taylor expansion, the fluence can be assumed to be quadratic in the point close to the intensity minimum:

$$\Phi(r) = \Phi_{\mathrm{HADES}}(r/a)^2, \tag{5}$$

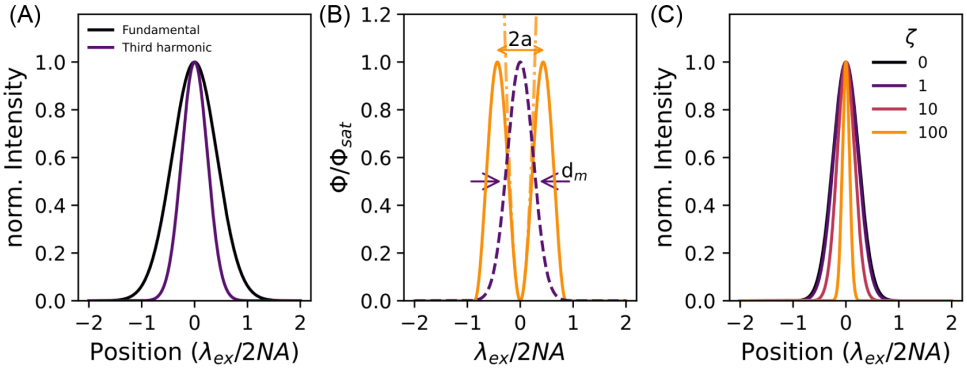

Fig. 2. (A) As described in (4), the point spread function (PSF) of the third harmonic reduces compared to the PSF of the fundamental NIR driver. The higher the effective nonlinear order, which also means the higher the harmonic order, the smaller the PSF. (B) Visualization of the geometric parameters for the donut (orange) and THG (purple) beam used in the equations. The donut center (solid) is approximated with a parabola (dashed-dotted). a is the distance from the center of the donut to the peak, while the FWHM of the THG is represented by d_m. For the ideal experimental deactivation, we chose $d_m/2a = 1$. (C) Adding the donut-shaped beam (inset), we see that a larger deactivation factor $\zeta = \Phi/\Phi_{\mathrm{sat}}$ leads to a smaller PSF. The case $\zeta = 0$ is equivalent to the THG in A.

where Φ_{HADES} and a are the experimentally applied fluence and radius at the maximum of the donut beam, respectively. We insert (5) into (1) to define a spatial emission efficiency function η_{em} after photoexcitation through a beam with deactivation factor $\zeta = \Phi_{\mathrm{HADES}}/\Phi_{\mathrm{sat},m}$ as

$$\eta_{\mathrm{em}}(r) = 1 - \delta(\Phi(r)) = \exp\left(-\ln(2)\zeta\left(\frac{r}{a}\right)^2\right). \quad (6)$$

We can neglect any form of carrier diffusion for two reasons, both ultimately caused by the short femtosecond pulses employed in HADES. First, the harmonic emission process itself is highly localized in real space [20,39]. Second, a combination of field effects and increased scattering rate suppresses the harmonics, both of which are highly local properties [33,34]. Intuitively, this can be understood as the HHG process happens within half an optical cycle [20] and the light excites carriers within a few femtoseconds [40,41]. Therefore, carrier diffusion in the sample does not take place as long as the two pulses sufficiently overlap temporally. Effectively, η_{em} acts as a soft aperture (Fig. 2C) in the near-field range of the sample. We can therefore describe the PSF of the whole setup by multiplying (6) with (3):

$$I_{\mathrm{HADES}}(r) \propto \exp\left[-4\ln(2)\frac{r^2}{d_m^2}\left(1+\left(\frac{d_m}{2a}\right)^2\zeta\right)\right]$$
$$\approx \exp\left[-4\ln(2)\frac{r^2}{d_m^2}(1+\zeta)\right]. \quad (7)$$

The diameter $2a$ in (7) can be omitted if $d_m/2a \approx 1$, which we motivate experimentally by looking at the cases when the diameter $2a$ is smaller or larger than the FWHM of the third-harmonic PSF, which coincides with the Abbe limit d_m. First, if $d_m/2a < 1$, the maximum deactivation moves outside of the HHG spot. This decreases the sharpness of the soft aperture and can be effectively modeled by decreasing the applied fluence. Second, if $d_m/2a > 1$, the maximum deactivation moves closer to the center of the HHG PSF, leading to wings on the outer edge, which is undesirable. The effective FWHM of the HHG intensity spot in HADES microscopy follows out of the FWHM of Eq. (7) as

$$d_{\mathrm{HADES},m} = \frac{\lambda_{\mathrm{ex}}}{2\mathrm{NA}\sqrt{m_{\mathrm{eff}}}}\frac{1}{\sqrt{1+\zeta}}. \quad (8)$$

This FWHM of the HHG emission spot in HADES is directly tied to resolution. The first term $\lambda_{\mathrm{ex}}/(2\mathrm{NA}\sqrt{m_{\mathrm{eff}}})$ in Eq. (8) is reminiscent of the Abbe limit for incoherent imaging, which is recovered in coherent imaging (which is the case for HHG microscopy) for non-interfering ($\pi/2$ out of phase) objects. The second term $1/\sqrt{1+\zeta}$ is the improvement in resolution via HADES with deactivation factor $\zeta = \Phi_{\mathrm{HADES}}/\Phi_{\mathrm{sat},m}$. Equation (8) thus shows that HADES can, in principle, provide unlimited resolution improvement as long as the deactivation factor can be optimized against the practical limitations, i.e., sample damage and intensity leakage as we show later. This can be achieved by applying high fluences in the orbital-angular momentum pulse Φ_{HADES}, and by finding strategies to achieve low fluences $\Phi_{\mathrm{sat},m}$ at which the HHG signal is suppressed.

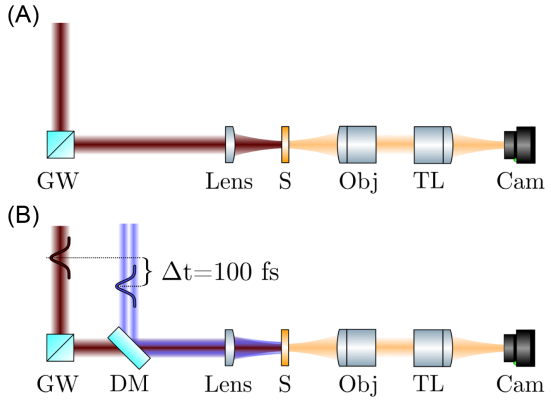

Fig. 3. Experimental setup. (A) Setup for the intensity scaling of single-color third-harmonic generation. (B) Setup for adding a second beam, which arrives 100 fs before the excitation pulse causes THG.

3. METHODS

In our experiments, we want to observe the reduction in FWHM of the emitted third harmonic. We used a pump-probe scheme (Fig. 3) to control the deactivation and a home-built microscope to image the resulting focal spots. We split light from a Ti:Sapphire laser into two arms. The first, called the excitation arm, generates NIR light in an optical parametric amplifier centered at 1800 nm. The second, called the deactivation arm, passes through a step phase plate which introduces an azimuthal 2π phase retardation, in order to imprint an OAM of 1 onto the beam. Telescopes in the two arms are used to overlap the focal spots of the two beams in space, while a motorized stage delays them in time. Both arms are recombined with a dichroic mirror and subsequently focused onto the sample using a 15 cm focal length lens. The two beams are linearly polarized and parallel to each other, although no strong polarization dependence of the HHG signal could be observed, presumably due to the polycrystalline thin films used in the present study.

For the results shown in Fig. 1, the step phase plate was omitted in the deactivation arm, and a Gaussian beam profile was used. The THG was collected by a fiber spectrometer. The temporal cross-correlation of the excitation and deactivation beam is measured to be 120 fs.

A microscope objective (Mitutoyo Apo NIR 20×, NA = 0.4) collects the transmitted harmonics, which are reimaged onto an sCMOS camera by a 25 cm focal length tube lens. This leads to an effective magnification of 25× of the microscope used. Bandpass filters, centered at 600 nm with a 40 nm bandwidth, were used to filter out the NIR excitation and pump light. The geometry of a (low-NA) focusing lens and a higher-NA objective was chosen to study the effect of HHG deactivation with OAM carrying pulses in a wide-field microscopy setting without the need for scanning samples.

The sample was a 115 nm NbO_2 thin film on a sapphire substrate. More information on the sample fabrication can be found in [32,42].

4. RESULTS

A. Single Beam PSF for Third-Harmonic Generation

We used only the 1800 nm beam in the first experiment to generate third harmonics in the NbO_2 thin film. At low input powers of

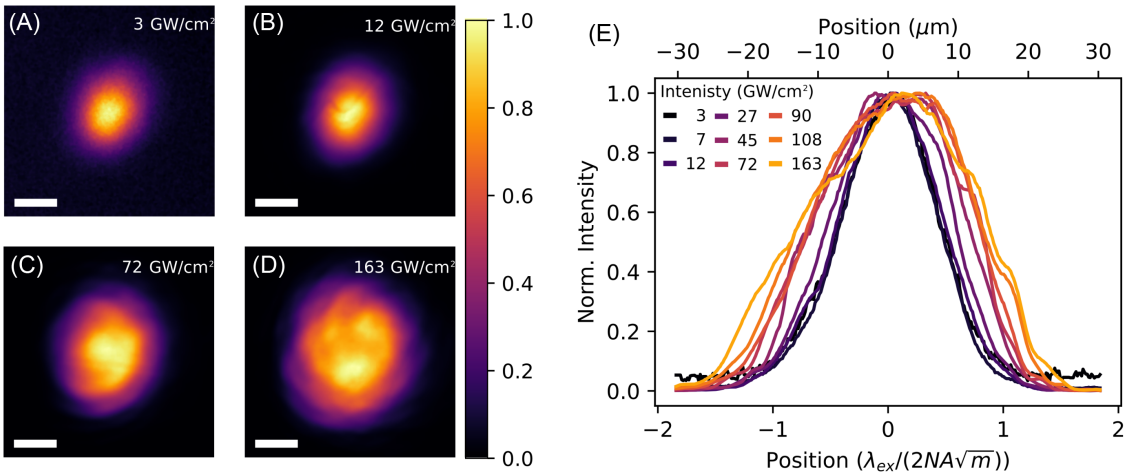

Fig. 4. PSF for THG: (A–D) microscope images of THG emission for varying excitation intensities. The scale bars are 10 μm. The PSF stays constant over an extended intensity range (A, B). For higher intensities, it becomes larger (C, D). (E) Lineouts from the emission profiles. In these lineouts, a transition from a Gaussian spot to a more irregular spot is visible with an increase in intensity.

the NIR driver, the spot shows a clear Gaussian profile as seen in Figs. 4A and 4B. Increasing the driver's power eventually increases the spot size and the emission becomes spatially more irregular (Figs. 4C and 4D). Hereby, the peak emission increases to a certain point until the wings start growing faster than the center. This phenomenon becomes visible when looking at lineouts at different powers (Fig. 4E). The lineouts are all normalized towards themselves, accounting for the harmonics' different emitted powers. For low powers, the lineouts stay identical, while for high powers, the imaged spots broaden gradually and get non-Gaussian.

Measuring the FWHM of the spots allows us to efficiently compare them to the predictions from (4). At first, the FWHM stays close to the diffraction limit for THG microscopy [Eq. (4)]. If the power increases, the perceived FWHM grows. This is predominantly linked to saturation of harmonic generation as a function of driving intensity, which generally occurs for harmonic generation due to both free-carrier absorption and state blocking. Resonant THG changes the effective refractive index worsening the phase matching [43]. Indeed, in Ref. [32] we observed a transition from an effective nonlinear order m_{eff} from 2.5 at low driving intensities to 1.2 at high intensities in Eq. (2) for THG from NbO_2. This means that for spatially resolved THG as shown in Fig. 4, the wings of the THG, which are generated with less driving intensity, will scale with a higher effective nonlinear order than the peak emission. We analyzed the intensity scaling in the wings, in the emission peak, and in the averaged beam profile, and plotted the results in a log-log scale in Fig. 5A. We indeed observe the expected behavior of a clear saturation in the peak emission which is visible as a change in slope in the log-log plot (orange line in Fig. 5A), while the slope of the averaged emission (black line in Fig. 5A) and particularly of the emission in the wings (purple line in Fig. 5A) change less. Strikingly, at intensities which saturate the harmonic emission a deviation from the predicated FWHM begins (Fig. 5B). Moreover, for the highest intensities, we cannot exclude that there is some background THG emission from the substrate. Such background emission would be out of focus of the imaging system, which would also make the observed THG larger.

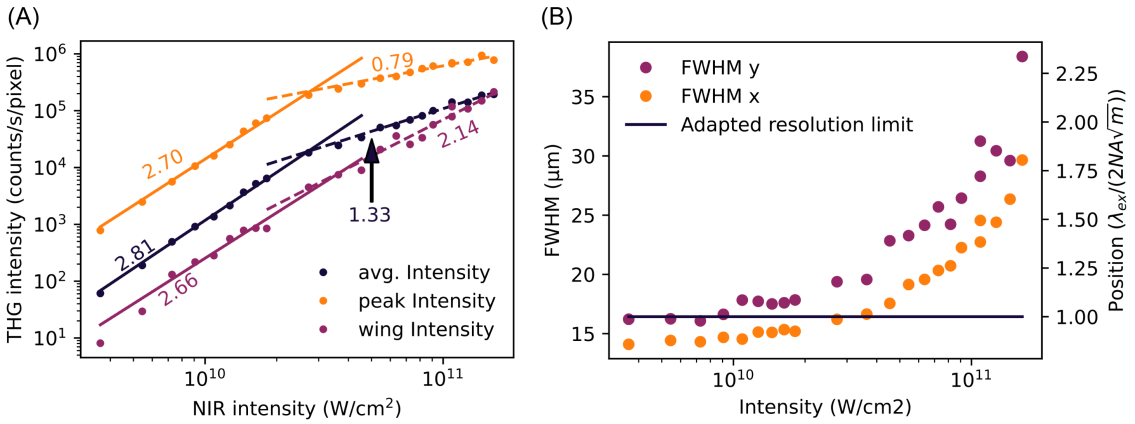

Fig. 5. Intensity and FWHM for THG: (A) scaling of the THG intensity versus the input NIR intensity on a log-log scale. We compare the average intensity (black) to the intensity in the center of the spot (orange) and on the wings of the spot (purple). The average and peak intensity go from a perturbative (solid) to a saturated regime (dashed), while the intensity in the wings keeps increasing until the damage threshold. Saturation is visible as a change in slope. The slopes are labeled in the figures. (B) FWHM of THG taken from results in Fig. 4 for varying excitation intensities. Initially, the point spread function remains constant over a whole order of magnitude in applied NIR intensity. After that, the spot steadily increases up to the damage threshold of the thin film.

To achieve the best resolution possible, we keep the input intensity as low as possible, while allowing for a sufficient signal-to-noise ratio. This will also yield the benefit that the second beam operates at higher fluences before laser damage occurs, thus allowing larger resolution improvements according to Eq. (8).

B. Dual Beam PSF for Reducing the PSF below the Diffraction Limit

We now study the reduction of the point-spread function when the second beam with a donut intensity profile in focus is added. The smallest PSF in the present experiment was always observed at a time difference of roughly 100 fs, compared to the maximum of the wave mixing signal which defines the time of optimum temporal pump-probe overlap. This corresponds to the maximum deactivation of the third-harmonic generation spectrum.

When looking at the point spread function, an immediate reduction can be seen, even when applying low fluences (Figs. 6A and 6B). This trend continues when increasing the power. Moreover, deactivation also visibly improves the circularity of the THG spot (Figs. 6C and 6D). We attribute this to the saturation style behavior, as even an imperfect donut beam for deactivation will lead to a total suppression of the harmonic emission at sufficient power. From the lineouts of the emitted harmonics at different powers of the donut beam (Fig. 6E), the continuous shrinking of the harmonic emission spot is more clearly visible. The FWHM of the PSFs from Fig. 6E is shown in Fig. 6F, where we observe a clear reduction of the FWHM, which is perfectly fit by the expression for the FWHM for HADES as described in Eq. (8). This result is directly linked to resolution in a confocal microscope, as elaborated in the following section. It should be noted that in Fig. 6, we used linearly polarized pulses for deactivation via a phase vortex, which causes a finite amount of intensity in the center of the donut-shaped pulses [44] in focus. We therefore renormalized the intensity in every image, as we see a 75% drop in peak emission for the highest pump power. A residual electric field in the center of our donut beam can explain this. Our simulation suggests that if the center has 5% of the peak fluence already, such a strong drop in peak THG can be seen. Furthermore, this drop in peak THG will result in a 13% larger FWHM. Improving the OAM pulse to feature a true zero intensity in the center would thus allow us to improve our resolution from currently four to extremely five times better than the Abbe limit. The fluence is translated from the Gaussian deactivation beam in Fig. 1 to the fluence in Fig. 6E according to Ref. [45].

5. DISCUSSION

We demonstrated control of the spot size of THG in single- and incommensurate two-color fields as well as for delayed pulses. In a single-color laser field, a change from the unsaturated to saturated generation regime is accompanied by an increase in the spot size.

We showed that adding a second laser pulse can deactivate the harmonic emission spatially and temporally, in a completely reversible fashion. Converting the deactivation beam to a donut-intensity shape decreases the emission spot size several times below the diffraction barrier. This improvement is only limited by the choice of parameters in the experiment and the laser-induced damage to the sample. In the current configuration, a reduction of the PSF was possible by a factor of 4. This spatial confinement of THG is suitable for achieving label-free super-resolution with ultrafast laser pulses via e.g., scanning far-field microscopy in a confocal microscope, called HADES. Our approach will also be beneficial to improve resolution in existing SHG or THG setup resolution, as shown in [16]. It is important to note that for incoherent imaging, these reductions in spot sizes would directly be related to the resolution of the system. However, THG and HHG imaging are coherent techniques [46,47], and in the present paper, we only

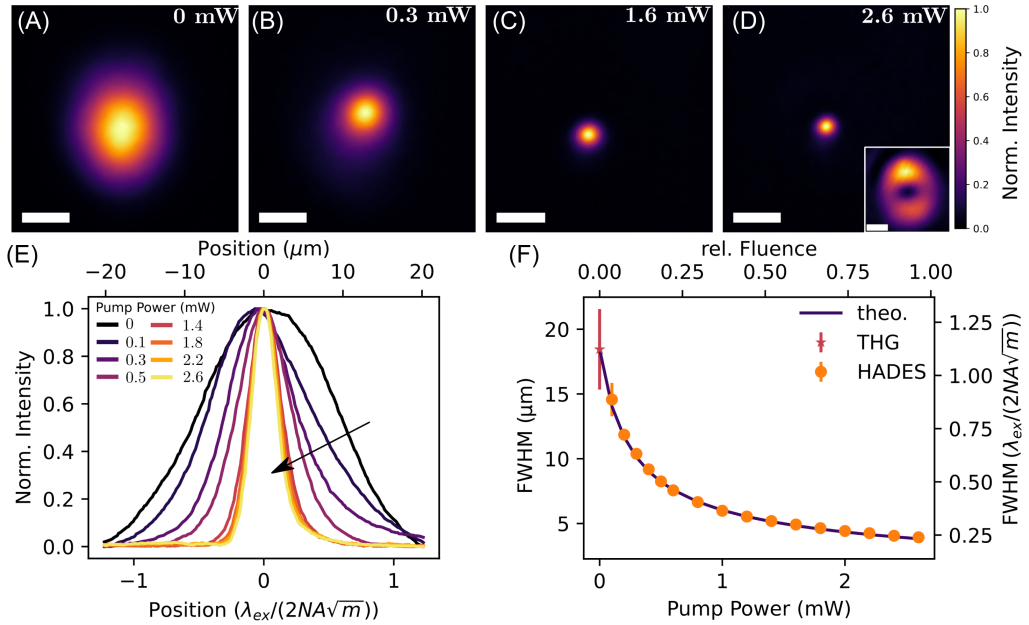

Fig. 6. PSF of HADES: (A–D) microscope images of THG emission spatially confined by a donut-shaped deactivation pulse (shown in the inset of D) for increasing average power, which leads to a rise of the deactivation fluence. The scale bars are 10 μm. Increasing the applied power of the donut deactivation beam decreases the FWHM of the THG spot (A–D). (E) Example lineouts along the horizontal direction show that increasing the donut beam's power decreases the spot size. (F) Extracted FWHM from lineouts in E, incl. a fit based on the HADES FWHM [Eq. (8)]. We achieve a fourfold spot size reduction.

measure the intensity PSF by imaging the emission profiles. For coherent imaging, the field PSF, which contains phase information, is a relevant quantity. To make accurate predictions of the resolution, we need to consider spatially separate objects that emit. In this case, the relative phase of the two emitters will also have an influence on the resolution. In the non-interfering case for a phase difference of $\pi/2$, the resolution for coherent imaging is the same as for incoherent imaging. The resolution for two objects is usually described by the Rayleigh limit $d_R = 0.61\lambda/\mathrm{NA}$ rather than the previously mentioned Abbe limit.

For constructive interference (0 phase difference), the addition of emitted fields blurs out the separation of the objects, and the resolution becomes worse by a factor of 1.34, giving a Rayleigh limit of $d_R = 0.83\lambda/\mathrm{NA}$. For destructive interference (π) two objects spaced by less than the resolution limit remain distinguishable. However, the measured separation remains diffraction limited [48] at $d_R = 0.83\lambda/\mathrm{NA}$.

The scaling of the resolution by HADES will remain the same as demonstrated in the present manuscript, meaning we expect up to a four times resolution improvement of a standard THG microscope for whichever phase difference between different emitting objects is present. Furthermore, although we used a long focal length lens in our experiments, the formula derived in (8) scales with the NA of the system. This means that we expect spot sizes of 140 nm for the THG using a dry objective with an NA of 0.95 and a driving wavelength of 1800 nm. Thus, 140 nm is the possible resolution for $\pi/2$ emitters, whereas for two emitters in phase, the resolution becomes 190 nm. We note that going to higher harmonics provides both better deactivation, i.e., a lower saturation fluence $\Phi_{\mathrm{sat},m}$, and a better intrinsic resolution due to a higher effective nonlinear order m_{eff}, which reduces the inherent HHG emission spot. For the data provided in [32], this makes sub-100 nm resolution via fifth-harmonic microscopy feasible. Even better resolution remains viable by finding explicit concepts for improving deactivation, i.e., lowering the deactivation fluence, or by efficiently preventing sample damage and thus being able to deactivate at higher peak fluences.

In order to fully implement HADES for super-resolution microscopy, two obstacles have to be overcome. We observed that the peak intensity of the emitted harmonics drops significantly during deactivation, suggesting a longitudinal electric field component in the center. A vectorial vortex beam or a phase vortex with circular polarization could prevent this longitudinal field component [44,49]. The second obstacle is that the fluence dictates the saturation effect and the damage threshold. By optimizing the deactivation mechanism that depends on the intensity of the donut beam rather than its fluence, we can decouple the damage threshold from the saturation effect. Especially, the accurate control of HHG in two-color laser fields [22,50–52] and more complicated fields [53] provides a promising tool for the universal application of HADES. New deactivation concepts for HHG will enable us to optimize the deactivation by e.g., controlling (shortening) the pulse duration, which will modify (increase) the peak intensity while having a constant fluence.

The PSF scaling presents a significant opportunity to enhance the resolution capabilities of THG microscopy, as demonstrated in [16]. Since the deactivation of HHG by synchronized or delayed prepulses has been observed in a variety of materials [25–31,33], there is an underlying generality: Deactivation is caused by suppression of electron-hole recollisions in an incommensurate field, and by increased carrier scattering and thus decreased electron-hole coherence in a photoexcited sample, as we have discussed in [33]. This provides confidence that HADES can become a generally applicable, label-free super-resolution technique, with the potential for temporal resolution on attosecond time scales.

Funding. Nederlandse Organisatie voor Wetenschappelijk Onderzoek (VI.Vidi223.133); HORIZON EUROPE European Research Council (101041819).

Acknowledgment. This work was conducted at the Advanced Research Center for Nanolithography (ARCNL), a public private partnership between the University of Amsterdam (UvA), Vrije Universiteit Amsterdam (VU), Rijksuniversiteit Groningen (RUG), the Dutch Research Council (NWO), and the semiconductor equipment manufacturer ASML, and was partly financed by "Toeslag voor Topconsortia voor Kennis en Innovatie (TKI)" from the Dutch Ministry of Economic Affairs and Climate Policy.

Disclosures. The authors declare no conflicts of interest.

Data availability. Data underlying the results presented in this paper are not publicly available at this time but may be obtained from the authors upon reasonable request.

REFERENCES

1. Y. M. Sigal, R. Zhou, and X. Zhuang, "Visualizing and discovering cellular structures with super-resolution microscopy," Science **361**, 880–887 (2018).
2. L. Schermelleh, A. Ferrand, T. Huser, *et al.*, "Super-resolution microscopy demystified," Nat. Cell Biol. **21**, 72–84 (2019).
3. N. Vuillemin, P. Mahou, D. Débarre, *et al.*, "Efficient second-harmonic imaging of collagen in histological slides using Bessel beam excitation," Sci. Rep. **6**, 29863 (2016).
4. M. Rehberg, F. Krombach, U. Pohl, *et al.*, "Label-free 3D visualization of cellular and tissue structures in intact muscle with second and third harmonic generation microscopy," PloS One **6**, e28237 (2011).
5. S. Witte, A. Negrean, J. C. Lodder, *et al.*, "Label-free live brain imaging and targeted patching with third-harmonic generation microscopy," Proc. Natl. Acad. Sci. USA **108**, 5970–5975 (2011).
6. D. Débarre, W. Supatto, A. M. Pena, *et al.*, "Imaging lipid bodies in cells and tissues using third-harmonic generation microscopy," Nat. Methods **3**, 47–53 (2006).
7. C. Heide, Y. Kobayashi, A. C. Johnson, *et al.*, "High-harmonic generation from artificially stacked 2D crystals," Nanophotonics **12**, 255–261 (2023).
8. C.-J. Kim, L. Brown, M. W. Graham, *et al.*, "Stacking order dependent second harmonic generation and topological defects in h-BN bilayers," Nano Lett. **13**, 5660–5665 (2013).
9. H. Ma, J. Liang, H. Hong, *et al.*, "Rich information on 2D materials revealed by optical second harmonic generation," Nanoscale **12**, 22891–22903 (2020).
10. F. Bijloo, K. Murzyn, F. van Emmerik, *et al.*, "Near-unity all-optical modulation of third-harmonic generation with a Fano-resonant dielectric metasurface," Nano Lett. **24**, 12942–12947 (2024).
11. R. Kolkowski, T. K. Hakala, A. Shevchenko, *et al.*, "Nonlinear nonlocal metasurfaces," Appl. Phys. Lett. **122**, 160502 (2023).
12. W. Liu, Z. Li, H. Cheng, *et al.*, "Dielectric resonance-based optical metasurfaces: from fundamentals to applications," iScience **23**, 101868 (2020).
13. T. L. Cocker, D. Peller, P. Yu, *et al.*, "Tracking the ultrafast motion of a single molecule by femtosecond orbital imaging," Nature **539**, 263–267 (2016).
14. S. A. Dönges, O. Khatib, B. T. O'Callahan, *et al.*, "Ultrafast nanoimaging of the photoinduced phase transition dynamics in VO_2," Nano Lett. **16**, 3029–3035 (2016).
15. A. S. Johnson, D. Perez-Salinas, K. M. Siddiqui, *et al.*, "Ultrafast X-ray imaging of the light-induced phase transition in VO_2," Nat. Phys. **19**, 215–220 (2023).
16. K. Murzyn, M. L. S. van der Geest, L. Guery, *et al.*, "Breaking Abbe's diffraction limit with harmonic deactivation microscopy," Sci. Adv. **10**, eadp3056 (2024).

17. T. A. Klar, S. Jakobs, M. Dyba, *et al.*, "Fluorescence microscopy with diffraction resolution barrier broken by stimulated emission," Proc. Natl. Acad. Sci. USA **97**, 8206–8210 (2000).
18. V. Westphal and S. W. Hell, "Nanoscale resolution in the focal plane of an optical microscope," Phys. Rev. Lett. **94**, 143903 (2005).
19. N. Dudovich, O. Smirnova, J. Levesque, *et al.*, "Measuring and controlling the birth of attosecond XUV pulses," Nat. Phys. **2**, 781–786 (2006).
20. S. Ghimire and D. A. Reis, "High-harmonic generation from solids," Nat. Phys. **15**, 10–16 (2019).
21. S. R. Abbing, F. Campi, F. S. Sajjadian, *et al.*, "Divergence control of high-harmonic generation," Phys. Rev. Appl. **13**, 054029 (2020).
22. S. D. Roscam Abbing, F. Campi, A. Zeltsi, *et al.*, "Divergence and efficiency optimization in polarization-controlled two-color high-harmonic generation," Sci. Rep. **11**, 24253 (2021).
23. P. M. Kraus, S. B. Zhang, A. Gijsbertsen, *et al.*, "High-harmonic probing of electronic coherence in dynamically aligned molecules," Phys. Rev. Lett. **111**, 243005 (2013).
24. P. M. Kraus, B. Mignolet, D. Baykusheva, *et al.*, "Measurement and laser control of attosecond charge migration in ionized iodoacetylene," Science **350**, 790–795 (2015).
25. Z. Wang, H. Park, Y. H. Lai, *et al.*, "The roles of photo-carrier doping and driving wavelength in high harmonic generation from a semiconductor," Nat. Commun. **8**, 1686 (2017).
26. C. Heide, Y. Kobayashi, A. C. Johnson, *et al.*, "Probing electron-hole coherence in strongly driven 2D materials using high-harmonic generation," Optica **9**, 512–516 (2022).
27. Y. Wang, F. Iyikanat, X. Bai, *et al.*, "Optical control of high-harmonic generation at the atomic thickness," Nano Lett. **22**, 8455–8462 (2022).
28. M. R. Bionta, E. Haddad, A. Leblanc, *et al.*, "Tracking ultrafast solid-state dynamics using high harmonic spectroscopy," Phys. Rev. Res. **3**, 023250 (2021).
29. Y. Cheng, H. Hong, H. Zhao, *et al.*, "Ultrafast optical modulation of harmonic generation in two-dimensional materials," Nano Lett. **20**, 8053–8058 (2020).
30. M. L. S. van der Geest, J. J. de Boer, K. Murzyn, *et al.*, "Transient high-harmonic spectroscopy in an inorganic–organic lead halide perovskite," J. Phys. Chem. Lett. **14**, 10810–10818 (2023).
31. Y. Wang, Y. Liu, P. Jiang, *et al.*, "Optical switch of electron-hole and electron-electron collisions in semiconductors," Phys. Rev. B **107**, L161301 (2023).
32. Z. Nie, L. Guery, E. B. Molinero, *et al.*, "Following the nonthermal phase transition in niobium dioxide by time-resolved harmonic spectroscopy," Phys. Rev. Lett. **131**, 243201 (2023).
33. P. J. van Essen, Z. Nie, B. de Keijzer, *et al.*, "Toward complete all-optical intensity modulation of high-harmonic generation from solids," ACS Photonics **11**, 1832–1843 (2024).
34. B. de Keijzer, P. J. van Essen, and P. M. Kraus, "Effect of photoexcitation on high-harmonic generation in semiconductors," J. Opt. Soc. Am. B **41**, 1754–1763 (2024).
35. G. Vampa, C. R. McDonald, G. Orlando, *et al.*, "Theoretical analysis of high-harmonic generation in solids," Phys. Rev. Lett. **113**, 073901 (2014).
36. P. Becker, H. Fragnito, C. B. Cruz, *et al.*, "Femtosecond photon echoes from band-to-band transitions in GaAs," Phys. Rev. Lett. **61**, 1647 (1988).
37. K. El Sayed, L. Bányai, and H. Haug, "Coulomb quantum kinetics and optical dephasing on the femtosecond time scale," Phys. Rev. B **50**, 1541–1550 (1994).
38. B. Harke, J. Keller, C. K. Ullal, *et al.*, "Resolution scaling in STED microscopy," Opt. Express **16**, 4154–4162 (2008).
39. H. Lakhotia, H. Y. Kim, M. Zhan, *et al.*, "Laser picoscopy of valence electrons in solids," Nature **583**, 55–59 (2020).
40. A. Schiffrin, T. Paasch-Colberg, N. Karpowicz, *et al.*, "Optical-field-induced current in dielectrics," Nature **493**, 70–74 (2013).
41. G. Wachter, C. Lemell, J. Burgdörfer, *et al.*, "Ab initio simulation of electrical currents induced by ultrafast laser excitation of dielectric materials," Phys. Rev. Lett. **113**, 087401 (2014).
42. Y. Wang, R. B. Comes, S. Kittiwatanakul, *et al.*, "Epitaxial niobium dioxide thin films by reactive-biased target ion beam deposition," J. Vac. Sci. Technol. A **33**, 021516 (2015).
43. H. Puell, H. Scheingraber, and C. R. Vidal, "Saturation of resonant third-harmonic generation in phase-matched systems," Phys. Rev. A **22**, 1165–1178 (1980).
44. N. Bokor, Y. Iketaki, T. Watanabe, *et al.*, "Investigation of polarization effects for high-numerical-aperture first-order Laguerre-Gaussian beams by 2D scanning with a single fluorescent microbead," Opt. Express **13**, 10440–10447 (2005).
45. C. Hnatovsky, V. G. Shvedov, W. Krolikowski, *et al.*, "Materials processing with a tightly focused femtosecond laser vortex pulse," Opt. Lett. **35**, 3417–3419 (2010).
46. Z. Tang, D. King, and S. Liu, "Imaging theory of nonlinear second harmonic and third harmonic generations in confocal microscopy," Sci. China G **47**, 8–16 (2004).
47. A. Aghigh, S. Bancelin, M. Rivard, *et al.*, "Second harmonic generation microscopy: a powerful tool for bio-imaging," Biophys. Rev. **15**, 43–70 (2023).
48. M. Born and E. Wolf, *Principles of Optics*, 7th (expanded) ed. (Syndicate of the University of Cambridge, 1999), Vol. **461**, pp. 401–424.
49. H. Yang, Y. Zhang, Y. Xiao, *et al.*, "Generation and comparison of donut-shaped depletion beams in STED microscopy," Optik **127**, 3735–3739 (2016).
50. M. Negro, C. Vozzi, K. Kovacs, *et al.*, "Gating of high-order harmonics generated by incommensurate two-color mid-IR laser pulses," Laser Phys. Lett. **8**, 875–879 (2011).
51. S. D. Roscam Abbing, N. Kuzkova, R. van der Linden, *et al.*, "Enhancing the efficiency of high-order harmonics with two-color non-collinear wave mixing in silica," Nat. Commun. **15**, 8335 (2024).
52. Z. Chen, M. Levit, Y. Kern, *et al.*, "Attosecond pulses from a solid driven by a synthesized two-color field at megahertz repetition rate," ACS Photonics **12**, 2819–2827 (2025).
53. O. Neufeld, D. Podolsky, and O. Cohen, "Floquet group theory and its application to selection rules in harmonic generation," Nat. Commun. **10**, 405 (2019).